Full Dose CT Database Induced Reconstruction With Nonlocal Means Prior for Ultra-Low-Dose Lung CT: A Preliminary Study

WENLEI LIU[1,2], PENG GAO[1], YUANKE ZHANG[1], TIANSHUAI LIU[1], HUANGSHENG PU[1], JUNYAN RONG[1], AND HONGBING LU[1]

[1]Department of Biomedical Engineering, Fourth Military Medical University, Xi'an 710032, China
[2]General Hospital of Western Theater Command, Chengdu 610083, China

Corresponding authors: Junyan Rong (junyanrong@126.com) and Hongbing Lu (luhb@fmmu.edu.cn)

ABSTRACT Although Low-dose computed tomography (LDCT) is the most effective way for early lung cancer screening, it's still a challenge to further reduce radiation dose on the premise of ensuring image quality. Penalized weighted least-squares (PWLS) image reconstruction with nonlocal means (NLM) prior has shown excellent performance to improve the image quality for LDCT, especially when the nonlocal weights are calculated from previous full-dose CT (FDCT) image. However, the previous FDCT image of the same patient is not readily available, and registration between the LDCT and FDCT images must be considered because of the scanning misalignment. This paper proposed a new NLM prior model to reconstruct high quality LDCT image without image registering. In order to estimate the nonlocal weights of NLM prior, a database was trained from FDCT images of different patients, from which the patch samples similar to each target patch of the LDCT were extracted. Then the nonlocal weights were determined by the patch samples, and integrated into PWLS reconstruction with the priori information of local structures from FDCT. Experiments with 10mAs LDCT data have shown its superiority in reducing noise, streaking artifacts and preserving structure detail, indicating the potential of further dose reduction in ultra-LDCT lung screening.

INDEX TERMS Ultra-low-dose lung CT, nonlocal means, penalized weighted least-squares, CT database.

I. INTRODUCTION

Lung cancer is the leading cause of cancer mortality around the world, with an estimation of 1.59 million deaths in 2012 [1]. The 5-year lung cancer survival rate is only 17.8% in the United States, and less than 18% in UK, Canada and China [1]–[3]. It can be greatly improved if lung cancer can be detected and diagnosed at its earlier stage in high-risk individuals. Currently, screening with low-dose computed tomography (LDCT) is the most effective way for early detection of lung cancer [4]–[7]. It has been proved a 20% reduction in lung cancer mortality with LDCT versus that of chest radiography by the National Lung Screening Trial (NLST), a massive study in the United States [8]. LDCT

shows its potential and benefits for early detection of lung cancer, but it's still a great risk exposing in the CT radiation. Most LDCT protocols for lung cancer screening have used scan parameters of 120-140 kVp and 30-100mAs, resulting in an average effective dose of 1.5 mSv [9]. It is 15 times as high as those delivered by the posteroanterior and lateral chest radiography of 0.1mSv [10]. Furthermore, the probable diagnostic chest CT or PET/CT increases the exposure, so as the annual LDCT for high-risk individuals [8], [11]. The accumulation of repeat scans increases the potential risk for radiation-induced cancer [12]. Therefore, ultra-low-dose CT (uLDCT) is needed for Lung cancer screening.

Currently, lowering the tube current–time product (mAs) is the main method to decrease the dose in lung cancer screening. The low-dose CT acquisition protocol often deteriorates the image reconstruction, due to the presence of

---

The associate editor coordinating the review of this manuscript and approving it for publication was Zhaoqing Pan.

noise and data insufficiency [13]. To mitigate this problem, the penalized weighted least-square (PWLS) criteria [14] has been proposed for LDCT reconstruction and shows superior performance in suppressing noise and streak artifacts. It models the signal-dependent noise properties with PWLS cost function provided that the noise in log-transformed projection data follows approximately Gaussian distribution and the variance of the noise can be determined by a formula showing the relationship between the mean transmission datum and the electronic noise [15], [16].

As well as the statistical noise model, the prior model also plays a critical role for effective reconstruction in LDCT [17]–[21]. The Markov random field (MRF) model-based priors have been widely used to promote the smoothness of the reconstructed image, assuming that the intensities of neighboring pixels are similar [21], [22]. To further improve spatial resolution, the nonlocal means (NLM) based prior has been successfully used as a penalty for the PWLS reconstruction, called PWLS-NLM [20], [23]. It utilizes redundancy information existed in images to calculate the nonlocal weight in a patch window for edge-preserving filtering. To improve the estimation accuracy of nonlocal weights, one way is to optimize NLM parameters such as the size of search window (SW) and patch window (PW), and smoothing parameter [24]. The other way is to use high-quality full-dose CT (FDCT) images with less noise and artifacts for better estimation of the weight [25]. Ma et al. designed a structure-preserving filter named ndiNLM, which utilized nonlocal means filtering induced from previous normal-dose scan of the same patient [26]. It shows promising gains in terms of noise reduction, low-contrast object detection and edge detail preservation. However, for lung cancer screening, the previous normal-dose CT scan of the same patient is not readily available. And registration should be required as the misalignment between low-dose and normal-dose scans could not be ignored, which may introduce uncertain errors. If nonlocal weights could be derived from high dose CT images of other patients, the practical significance of PWLS-NLM in lung cancer screening could be greatly strengthened.

Except for the FDCT based reconstruction, the FDCT based image restoration also works. Zhang et al proposed an adaptive prior features assisted (APFA) restoration scheme for low dose CT lung images [27]. Based on an offline training database consisting of patch samples extracted from existing full-dose lung scans, the APFA integrated the patch-search scheme with principal components analysis to retrieve local structure and texture pattern adaptively for the LDCT target. The results show that it can achieve a noticeable gain over some state-of-the-art methods in terms of noise suppression and details/textures preservation. However, its performance would be limited when applied to uLDCT images with serious noise and artifacts.

In this study, we proposed a new NLM prior and integrated it into the PWLS framework for potential lung cancer screening with ultra-low-dose CT, which was based on a training database from FDCTs. Assuming the accuracy of nonlocal weights could be related to the similarity degree of the patches in the search window, the patch samples from FDCT training database would be great help for improving the weights accuracy. When the nonlocal weights were extracted as the most similar patch samples from FDCT database, the structure detail or texture of reconstructions should be improved further, and the prior FDCTs should not be restricted to the same patient and the registration process could be skipped directly.

The rest of this paper is organized as follows. In section II, the training database-based patches for the NLM prior in the PWLS algorithm (PWLS-NLMpatch) is presented in details and the comparative and evaluation methods are presented. Section III reports the experimental results with artificial low dose CT data based on real CT data. Finally, discussions and conclusions are given in section IV and V.

II. MATERIALS AND METHODS
A. REVIEW OF THE PWLS RECONSTRUCTION WITH NLM PRIOR (PWLS-NLM)

The PWLS cost function of CT imaging can be expressed as follows:

$$\boldsymbol{\mu}^* = \arg\min_{\boldsymbol{\mu}} \left\{ (y - \mathbf{A}\boldsymbol{\mu})^T \Sigma^{-1} (y - \mathbf{A}\boldsymbol{\mu}) + \beta \mathrm{U}(\boldsymbol{\mu}) \right\}, \quad (1)$$

where y is the vector of measured line integral, $\mathbf{A}$ is the system matrix, T is a transpose operator, $\boldsymbol{\mu}$ is the vector of image to be reconstructed and Σ is a diagonal matrix with the i_{th} element of $\sigma_{y_i}^2$, which is the variance of y_i. It can be determined by the following mean-variance relationship in consideration of both X-ray quanta noise and system electronic noise [15], [16], [24]:

$$var(y_i) = \sigma_{y_i}^2 = \frac{\bar{N}_i + \sigma_e^2}{\bar{N}_i^2} = \frac{1}{\bar{N}_{0i}^2} \exp(\bar{y}_i)(1 + \frac{\sigma_e^2}{\bar{N}_{0i}} \exp(\bar{y}_i)),$$
$$(2)$$

where $\bar{N}_{0i}$ and $\bar{N}_i$ represent the mean number of X-ray photons transmitting before and after the patient respectively, which can be detected by detector bin i.

For the second term of equation (1), $\mathrm{U}(\boldsymbol{\mu})$ denotes the penalty term and β is a smoothing parameter which controls the tradeoff between the data fidelity and the penalty term. In NLM, a patch which is modeled as a pixel and its $K \times K$ nearest neighbors, is used to reflect local spatial structure of a pixel. For the PWLS-NLM algorithm, $\mathrm{U}(\boldsymbol{\mu})$ can be expressed as equation (3) [24], where ϕ denotes a positive potential function and can be chosen as quadratic function $\phi(\Delta) = \frac{1}{2}\Delta^2$. The weighting coefficient $\omega_{jk}(\boldsymbol{\mu})$ is calculated from $\boldsymbol{\mu}$, the image to be reconstructed. $\mathrm{P}(\mu_j)$ denotes the patch centered at pixel j; h is the filtering parameter and a is the standard deviation of the Gaussian kernel. The similarity between pixels j and k depends on the weighted Euclidean

distance of their patches.

$$U(\boldsymbol{\mu}) = \sum_j (\phi(u_j - \sum_{k \in SW_j} \omega_{jk}(\boldsymbol{\mu})u_k),$$

$$and \ \omega_{jk}(\boldsymbol{\mu}) = \frac{\exp(-\|\mathbf{P}(u_j) - \mathbf{P}(u_k)\|^2_{2,a}/h^2)}{\sum_{k \in SW_j} \exp(-\|\mathbf{P}(u_j) - \mathbf{P}(u_k)\|^2_{2,a}/h^2)}, \quad (3)$$

In repeated CT scans, a previously scanned FDCT image has lower noise and higher resolution than the current LDCT image, and majority of the anatomical information are same between the two scans. The PWLS-ndiNLM algorithm utilize fully the redundancy of information in the prior image to construct the NLM regularization. It is written as:

$$U(\boldsymbol{\mu}) = \sum_j (\phi(u_j - \sum_{k \in SW_j} \omega_{jk}(\boldsymbol{\mu}^{FD}, \boldsymbol{\mu})u_k^{FD}),$$

$$and \ \omega_{jk}(\boldsymbol{\mu}^{FD}, \boldsymbol{\mu}) = \frac{\exp(-\|\mathbf{P}(u_j) - \mathbf{P}(u_k^{FD})\|^2_{2,a}/h^2)}{\sum_{k \in SW_j} \exp(-\|\mathbf{P}(u_j) - \mathbf{P}(u_k^{FD})\|^2_{2,a}/h^2)},$$

$$(4)$$

where the weighting coefficient $\omega_{jk}(\boldsymbol{\mu}^{FD}, \boldsymbol{\mu})$ is calculated from the full dose image and the reconstructed image of $\boldsymbol{\mu}$. $\mathbf{P}(u_k^{FD})$ denotes the patch centered at pixel k from FDCT, $\mathbf{P}(u_j)$ denotes the patch centered at pixel j from the image to be reconstructed, and $\|\mathbf{P}(u_j) - \mathbf{P}(u_k^{FD})\|^2_{2,a}$ calculates the similarity between the patch of pixel j and the patch of pixel k.

In PWLS-ndiNLM, the nonlocal weights are determined by the similarity between the target patch and similar patches from the search window of the FDCT image. Once there is no FDCT image, the algorithm cannot work.

B. PWLS RECONSTRUCTION WITH NLM PRIOR BASED ON PATCHES FROM TRAINING DATABASE OF FDCTS (PWLS-NLMPATCH)

Inspired by the APFA algorithm [27], we proposed a new NLM prior model incorporated into the PWLS framework, where all patches in the search window consist of samples from the training database. The training database was constructed offline and the construction process was similar to that of APFA [27]. To build the training database, full-dose lung scans were first collected from different patients. For each patient's FDCT scan, 2D patches of size K × K were extracted automatically with a sliding distance of one pixel on the FDCT image. Then all the patches from different patients were stacked into a training database, denoted by $\boldsymbol{\mu}^{DB}$. The nearest similar patches DB_j are determined by evaluating the similarity (Euclidean distance) between patches from $\boldsymbol{\mu}^{DB}$ and the target patch $\mathbf{P}(u_j)$ of LDCT. How to decide the scale of the training database and the DB_j will be discussed in the experiments part.

So, the second term in ϕ of equation (4) is determined by similar patches selected from a FDCT training database,

as shown below:

$$U(\boldsymbol{\mu}) = \sum_j (\phi(u_j - \sum_{k \in DB_j} \omega_{jk}(\boldsymbol{\mu}^{DB}, \boldsymbol{\mu})u_k^{DB}),$$

$$\omega_{jk}(\boldsymbol{\mu}^{DB}, \boldsymbol{\mu}) = \frac{\exp(-\|\mathbf{P}(u_j) - \mathbf{P}(u_k^{DB})\|^2_{2,a}/h^2)}{\sum_{k \in DB_j} \exp(-\|\mathbf{P}(u_j) - \mathbf{P}(u_k^{DB})\|^2_{2,a}/h^2)}, \quad (5)$$

where the weighting coefficient $\omega_{jk}(\boldsymbol{\mu}^{DB}, \boldsymbol{\mu})$ is calculated from the training database (DB) of $\boldsymbol{\mu}^{DB}$ and the reconstructed image of $\boldsymbol{\mu}$. The NLM filtering pixel of μ_j is calculated as $\sum_{k \in DB_j} \omega_{jk}(\boldsymbol{\mu}^{DB}, \boldsymbol{\mu})u_k^{DB}$, where DB_j denotes the nearest similar patches in $\boldsymbol{\mu}^{DB}$ to the target patch $\mathbf{P}(u_j)$ with center pixel μ_j and $\mathbf{P}(u_k^{DB})$ denotes the patch centered at pixel k of $\boldsymbol{\mu}^{DB}$.

In summary, the cost function for the proposed PWLS-NLMpatch can be rewritten as:

$$\boldsymbol{\mu}^* = \arg\min_{\boldsymbol{\mu}} \left\{ (y - \mathbf{A}\boldsymbol{\mu})^T \Sigma^{-1} (y - \mathbf{A}\boldsymbol{\mu}) \right.$$

$$\left. + \beta \sum_j \frac{1}{2} (u_j - \sum_{k \in DB_j} \omega_{jk}(\boldsymbol{\mu}^{DB}, \boldsymbol{\mu})u_k^{DB})^2 \right\}, \quad (6)$$

C. FLOWCHART SUMMARY OF THE PROPOSED PWLS-NLMPATCH METHOD

The flowchart of the PWLS-NLMpatch is summarized as follows:

Step 1: Produce an initial image $\hat{\mathbf{u}}$ by FBP or other reconstruction algorithms. Initiate the following formulae:

$$\mathbf{q} = \mathbf{A}\hat{\mathbf{u}}, \quad \hat{\mathbf{r}} = \mathbf{y} - \mathbf{q}, \ \mathbf{D} = diag(1/\sigma_{y_i}^2), \quad (7)$$

Step 2: Construct offline training database with FDCTs from different patients. Step1 and Step2 can be exchanged with each other.

Step 3: For each target patch of the LDCT, select similar patch samples from the training database. The effect of selective patch samples in the PWLS-NLMpatch algorithm is same as that of patches in the search window in the PWLS-ndiNLM or the PWLS-NLM algorithms.

Step 4: Apply the empirical one-step-late (OSL) implementation and the Gauss-Seidel (GS) updating strategy for the reconstruction [20]. The reconstruction is updated iteratively by minimizing the cost function (6) according to equation (8) and would be ended if the stop criterion is satisfied.

$$u_j^{new} = \frac{\mathbf{A}_j^T \mathbf{D}\hat{\mathbf{r}} + \lambda_j u_j^{old} + \beta \sum_{k \in DB_j} \omega_{jk}(\boldsymbol{\mu}^{DB}, \boldsymbol{\mu})u_k^{DB}}{\lambda_j + \beta}, \quad (8)$$

where $\lambda_j = \mathbf{A}_j^T \mathbf{D}\mathbf{A}_j$ and $\mathbf{A}_j$ denotes the j_{th} column of the system matrix A. The parameters of PW size, DB_j size, h, a, and β are determined according to published papers [20], [21], [28].

D. COMPARATIVE METHODS AND EVALUATION MERITS

In order to evaluate the performance of PWLS-NLMpatch, both the PWLS-ndiNLM and PWLS-NLM algorithms were used for comparison, considering they are typical algorithms to be compared. It is verified that the former can achieve close-to-optimal results in the current state of the art. However, it needs full dose scan of the same patient and will increase the potential dose risk. The PWLS-NLM algorithm only utilizes information of the current scan for the regularization, overcoming the dose problem of the PWLS-ndiNLM. However, the current LDCT with high noise and streaking artifacts may affect the reconstruction accuracy of the PWLS-NLM.

Quantitative merits of root mean square error (RMSE), universal quality index (UQI) were utilized to evaluate the performance of the reconstruction algorithms. Let $\mathbf{X}_r = (x_{r,1}, x_{r,2} \ldots x_{r,J})^T$ denotes the vector of reconstructed image and $\mathbf{X}_0 = (x_{0,1}, x_{0,2} \ldots x_{0,J})^T$ denotes the vector of the ground truth image. The RMSE is employed to reflect the difference between the reconstructed image and the ground truth for regions of interest (ROI). It is formulated as equation (9):

$$\text{RMSE} = \sqrt{\frac{1}{Q} \sum_{j=1}^{j=Q} (x_{r,j}^{roi} - x_{0,j}^{roi})^2} \qquad (9)$$

where Q is the number of pixels in the ROI. The smaller the RMSE is, the nearer for the ROI to the ground truth.

The UQI was to quantify the similarity of noise, spatial resolution and texture correlation between the reconstructed image and the ground truth in the ROIs. It is defined as equation (10):

$$UQI = \frac{4cov(\mathbf{x}_r^{roi}, \mathbf{x}_0^{roi})}{var(\mathbf{x}_r^{roi}) + var(\mathbf{x}_0^{roi})} \cdot \frac{\bar{\mathbf{x}}_r^{roi} \cdot \bar{\mathbf{x}}_0^{roi}}{(\bar{\mathbf{x}}_r^{roi})^2 + (\bar{\mathbf{x}}_0^{roi})^2},$$

$$var(\mathbf{x}_r^{roi}) = \frac{1}{Q-1} \sum_{j=1}^{Q} (x_{r,j}^{roi} - \bar{\mathbf{x}}_r^{roi})^2,$$

$$var(\mathbf{x}_0^{roi}) = \frac{1}{Q-1} \sum_{j=1}^{Q} (x_{0,j}^{roi} - \bar{\mathbf{x}}_0^{roi})^2,$$

$$cov(\mathbf{x}_r^{roi}, \mathbf{x}_0^{roi}) = \frac{1}{Q-1} \sum_{j=1}^{Q} (x_{r,j}^{roi} - \bar{\mathbf{x}}_r^{roi})(x_{0,j}^{roi} - \bar{\mathbf{x}}_0^{roi}) \quad (10)$$

where, $\bar{\mathbf{x}}_r^{roi}$ and $\bar{\mathbf{x}}_0^{roi}$ are the mean values of the Q pixels in the ROIs of the reconstructed image and the ground truth respectively. The higher the UQI is, the more like the ground truth in terms of noise, spatial resolution and texture correlation.

Except for the above quantitative merits, the line spread function (LSF) was analyzed to evaluate the spatial resolution of the reconstructed images, which was estimated from the edge spread function (ESF) [29]. In addition, the normal vector flow (NVF) [21], [27] was plotted to evaluate the texture similarity on selective ROIs. The gradual changes of the intensities in the desired image are often shown as ordered arrow in the NVF image, while the noise in the image is often shown as disordered arrows. The NVF image of the ROI image in the FDCT from the same patient was served as ground truth. The NVF images of the same ROI in LDCT reconstructions with different algorithms were compared to the ground truth. The best matched NVF demonstrates the fine textures are better preserved.

E. DATA ACQUISITION AND SIMULATION DESIGN

We validated the proposed reconstruction method with acquired FDCT data and artificial LDCT data based on real data. Under informed consents after the approval by the Institutional Review Board, three patients (denoted as patient #1 to patient #3) were recruited with full-dose scans acquired from clinical CT-guided lung nodule needle biopsy studies. The FDCT data were acquired from a Siemens CT scanner with 120 kVp tube voltage and 100 mAs tube current using a fan-beam geometry. The source-to-detector distance was 1040 mm, the source-to-axis distance was 570 mm, and 1160 projection views were evenly spanned on a 360° circular orbit. The detector bin spacing was 1.407 mm. The FDCT images (denoted as FDCT #1 to FDCT #3) were reconstructed by the traditional FBP algorithm with hundreds of slices.

The LDCT data for patient #3 was simulated with 10 mAs based on the FDCT projection data of patient #3. The imaging geometry in the LDCT simulation was the same as that of FDCT acquisition. Also, it is assumed that the detected pre-logarithm X-ray intensity follows the Poisson process plus the electronic noise background, which has been verified [15]. Firstly, the noise-free sinogram y was obtained by computing the line integration of the attenuation coefficients using equation (11):

$$y = \mathbf{A}\boldsymbol{\mu} \qquad (11)$$

Then the simulated noisy CT transmission data b_i at each detector bin i was generated according to the statistical model of pre-logarithm projection data:

$$b_i = \text{Possion}(I_0 \exp(-y_i)) + \text{Normal}(0, \sigma_e^2) \qquad (12)$$

where I_0 denoted the incident X-ray intensity and σ_e^2 was the background electronic noise variance. The noisy sinogram data $\tilde{y}_i$ were calculated by performing the logarithm transformation on the transmission data b_i. All of the LDCT data were computed by setting I_0 as the actual X-ray intensity collected at 10mAs and the electronic noise variance σ_e^2 as 10.

With the acquired FDCT data and the simulated LDCT data, two slices (slice #22 and slice #6) of patient #3 shown in figure 1 were reconstructed separately, to evaluate and validate the proposed PWLS-NLMpatch algorithm, compared to other algorithms. For the PWLS-NLMpatch algorithm, the training database was constructed from FDCT of patient #1 and/or patient #2.

III. RESULTS

A. COMPARISON BETWEEN DIFFERENT ALGORITHMS

Reconstruction results for slice #22 and slice #6 of patient #3 by the PWLS algorithms with general NLM prior
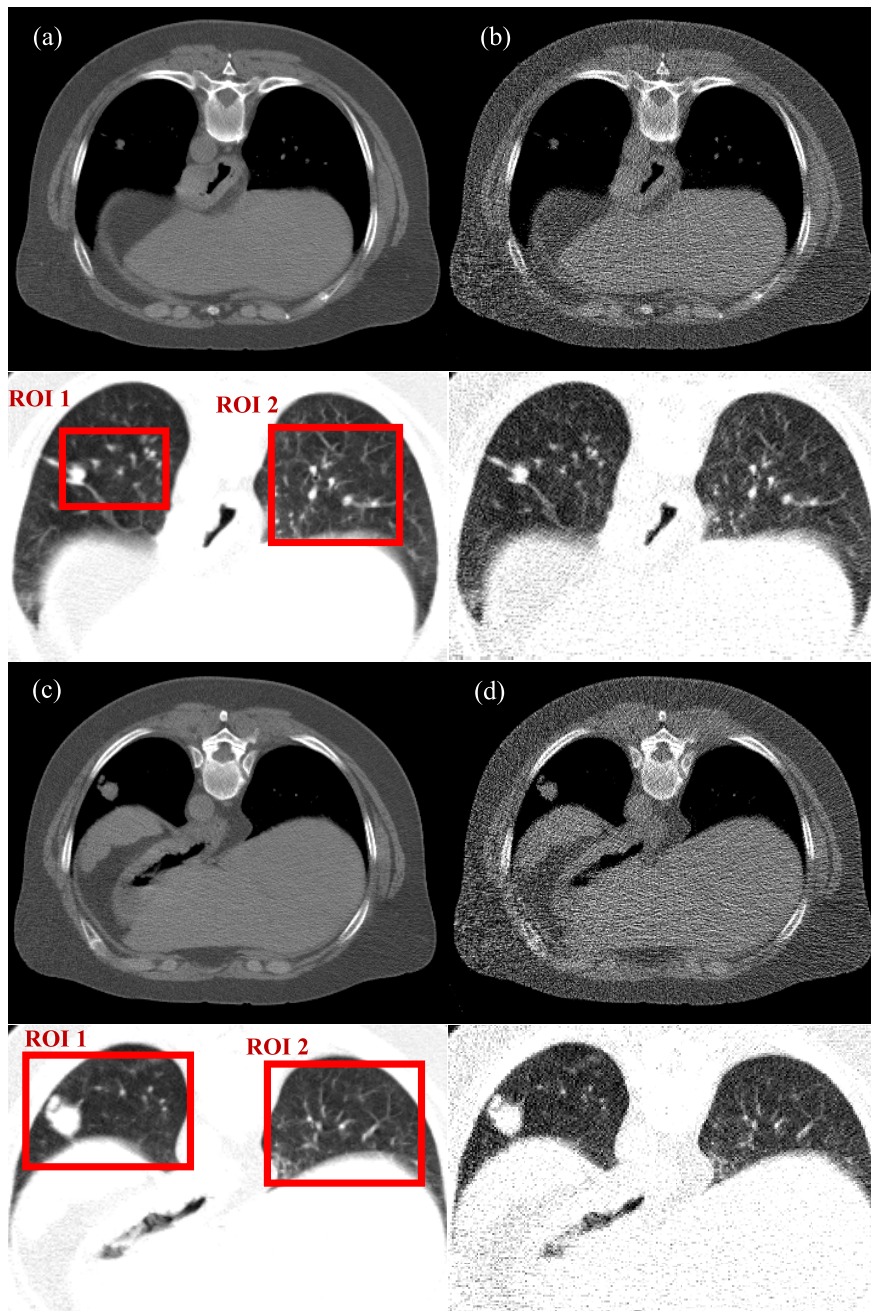
FIGURE 1. Two slices of images from patient #3 for studying. Both of them are reconstructed with the FBP algorithm. Slice #22 is shown in the first and second rows and slice #6 is shown in 3-4 rows. Both slices are shown firstly on a line with a window of [0.0112, 0.0288] mm^{-1} for better displaying the mediastinum and bone structure, and then with a lung display window of [0, 0.0220] mm^{-1} for their enlarged lung regions on the next line. The Left column are the FDCT images and the right column are the corresponding LDCT images (denoted as FDCT-FBP and LDCT-FBP respectively).

(PWLS-NLM), the normal-dose scan induced NLM prior (PWLS-ndiNLM) and the proposed training database-based NLM prior (PWLS-NLMpatch) are compared in Figure 2. For PWLS-NLMpatch algorithm, image was reconstructed with h of 0.003, β of 1×10^6 and 343382 patches constructed from FDCT of patient #1 and patient #2. For comparison, in PWLS-ndiNLM algorithm, h and β were set similar to

that of PWLS-NLMpatch. However, when reconstructing with PWLS-NLM algorithm with the same h, high distortion around the edge area of the image exist. Therefore, h was set as 0.01 in PWLS-NLM algorithm, which was determined experimentally, when there was no apparent deformation in vision. Figure 2 demonstrates that all PWLS reconstructions with the NLM based priors have improvement in
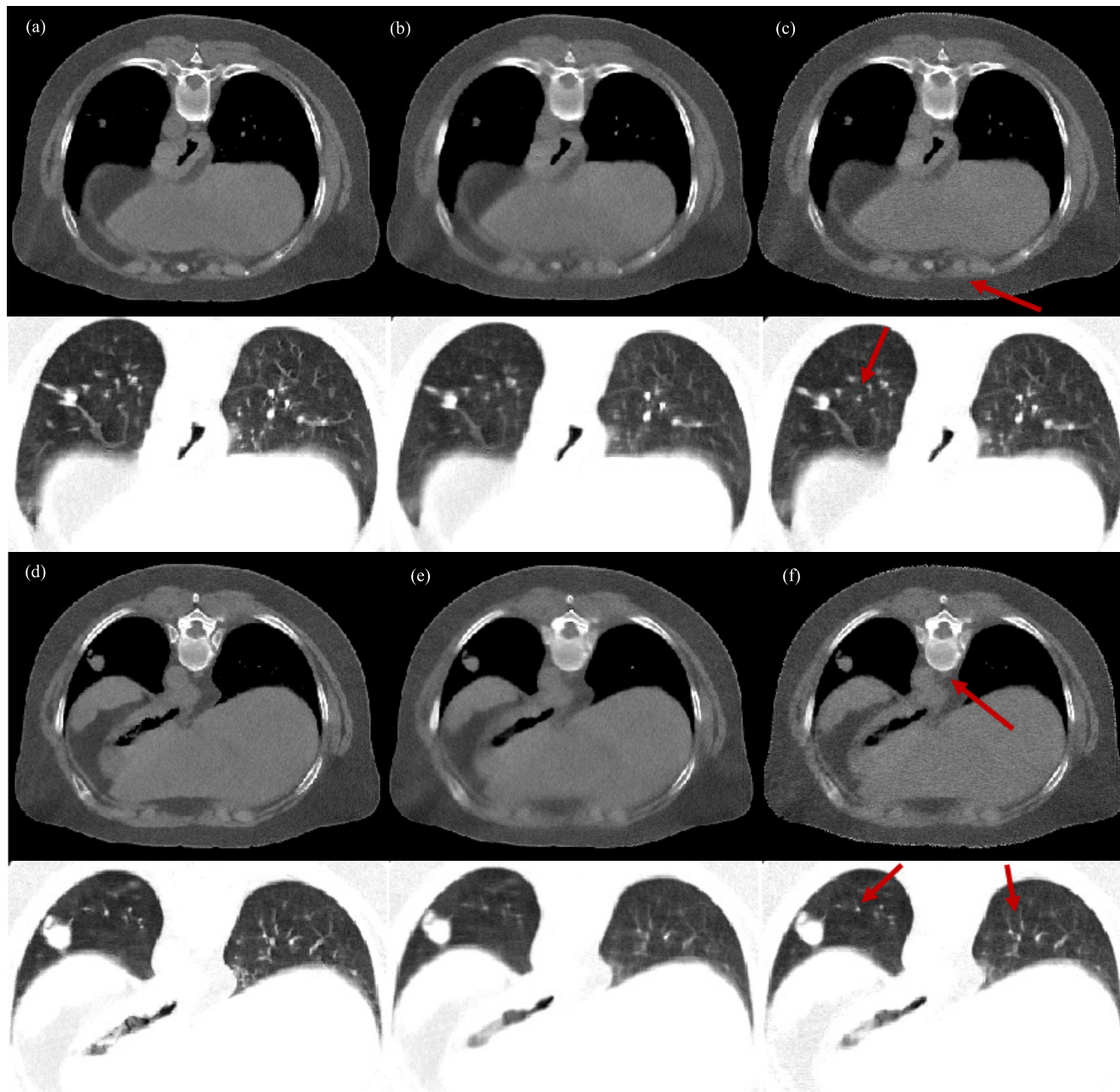
FIGURE 2. Reconstructions of slice #22 and slice #6 with different algorithms. The first and second rows are reconstructions of slice #22 while the third and fourth rows are reconstructions of slice #6. The columns from left to right are the PWLS-ndiNLM, PWLS-NLM and the PWLS-NLMpatch images. Both slices are shown firstly with a window of [0.0112, 0.0288] mm^{-1} for better displaying the mediastinum and bone structure, and then with a lung display window of [0, 0.0220] mm^{-1} for their enlarged lung regions on the next line.

suppressing noises, compared to the LDCT-FBP results in Figure 1. From the red arrows in Figure 2, we can see the proposed model is better than the conventional NLM prior in lung detail preservation, although it is not as good as the PWLS-ndiNLM. To further reflect the differences between reconstructed images, horizontal profiles of the resulting images were drawn in Figure 3. Profile of the FDCT-FBP was plotted as reference. Compared to PWLS-NLM image, the PWLS-ndiNLM and PWLS-NLMpatch images generate profiles closer to the reference. The PWLS-NLMpatch images

are improved compared to the PWLS-NLM images, although they are a little worse than the PWLS-ndiNLM reconstructions. The quantitative merits with RMSE and UQI for the ROIs shown in Figure 1 are presented in Table 1 and Table 2, reflecting the same conclusion as the visual and profile result.

The LSF and fitting curves along the horizontal and vertical directions for slice #22 and slice #6 were plotted in Figure 4. The FDCT-FBP was for reference. Apparently, the LSF curves of PWLS-NdiNLM are the closest to the reference curves. The LSF curves of the PWLS-NLMpatch
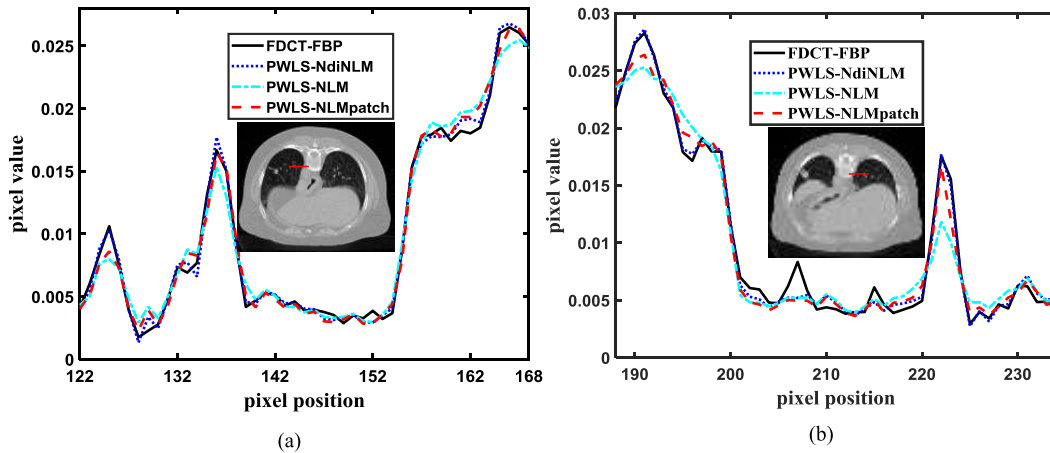
FIGURE 3. Horizontal profiles of the images reconstructed with different methods. The left is for slice #22 and the right is for slice #6. The profiles are along the red lines shown in the imbedded images.

TABLE 1. The RMSE and UQI of the ROIs shown in figure 2 for slice #22 using different algorithms.

Parameters	ROIs	LDCT-FBP	PWLS-ndiNLM	PWLS-NLM	PWLS-NLMpatch
RMSE	ROI1	11.2	6.03	8.90	7.90
(10^{-4})	ROI2	11.1	6.88	9.38	7.78
UQI	ROI1	1.7426	1.9428	1.8909	1.9456
	ROI2	1.8124	1.9496	1.8975	1.9317

TABLE 2. The RMSE and UQI of the ROIs shown in Figure 2 for slice #6 using different algorithms.

Parameters	ROIs	LDCT-FBP	PWLS-ndiNLM	PWLS-NLM	PWLS-NLMpatch
RMSE	ROI1	22.8	6.48	9.09	8.85
(10^{-4})	ROI2	17.2	6.00	9.43	8.37
UQI	ROI1	1.9149	2.0021	1.9923	1.9950
	ROI2	1.9412	1.9971	1.9831	1.9913

are narrower than that of the PWLS-NLM, and some of them are similar to that of the PWLS-NdiNLM. It suggests the improvement of the proposed model on edge preservation. In order to evaluate the texture similarity, the NVF images of the selected ROI of slice #22 (Figure 5 (a)) were drawn in Figure 5. The NVF image of the FDCT-FBP (Figure 5 (b)) was shown as the ground truth. Figure 5(c) shows the NVF image of the LDCT-FBP reconstruction, where strong noise exists. Figure 5(d)-(f) show the NVF images of the reconstructions with PWLS-NdiNLM, PWLS-NLM and PWLS-NLMpatch, respectively. We can observe that for the selected ROI, all the PWLS algorithms with the NLM based prior can suppress the disordered arrows in the uniform regions. The ordered arrows in the NVF image with the PWLS-ndiNLM method matched best to the ground truth, while that with the proposed algorithm was a litter worse than the PWLS-ndiNLM, but better than the PWLS-NLM method, especially in the blue ellipse regions.

B. COMPARISON BETWEEN DIFFERENT ALGORITHMS

1) THE QUALITY OF INITIAL IMAGE

The patches DB_j similar to the target patch were obtained based on the initial image and the training database in the PWLS-NLMpatch algorithm. With the same training database, the quality of the initial image plays an important role in the reconstruction. The reconstructions with two kinds of initial images are shown in Figure 6. First is the LDCT-FBP reconstruction (Figure 6 (a)), which presents high noise and artifacts. Second is the filtered LDCT-FBP with NLM filtering (denoted as NLMimage, Figure 6 (b)) with parameters of patch window =5, search window =17, and smoothing parameter of 0.005. Figure 6 (c)-(d) are the PWLS-NLMpatch reconstructions using them as initial images, respectively. From the red arrows shown in Figure 6, it demonstrated that the reconstruction with NLMimage as initial image was improved in reducing noise, although there may be a little loss of resolution and detail.
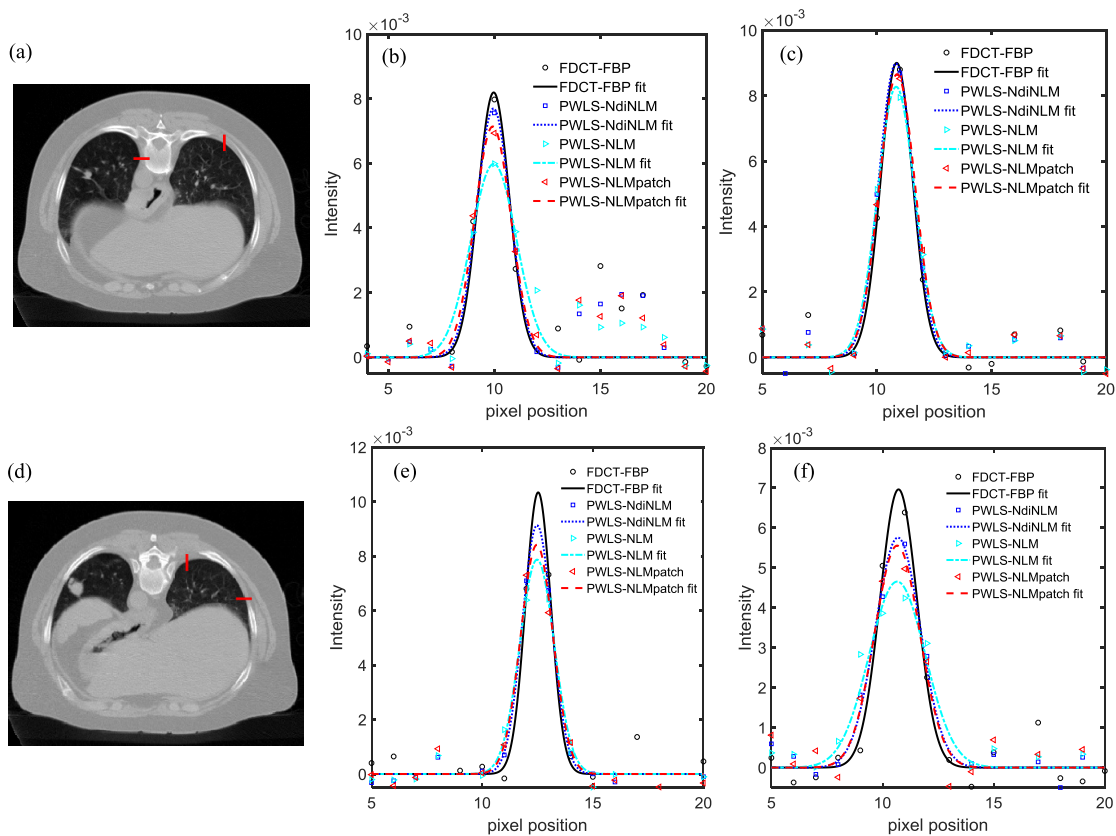
FIGURE 4. Horizontal and vertical LSF curves of images reconstructed using different algorithms. 1st row: slice #22; 2nd row: slice #6. Left column: the reconstructed images with red lines of horizontal and vertical directions for the corresponding LSF curves; middle column: horizontal resolution; right column: vertical resolution.
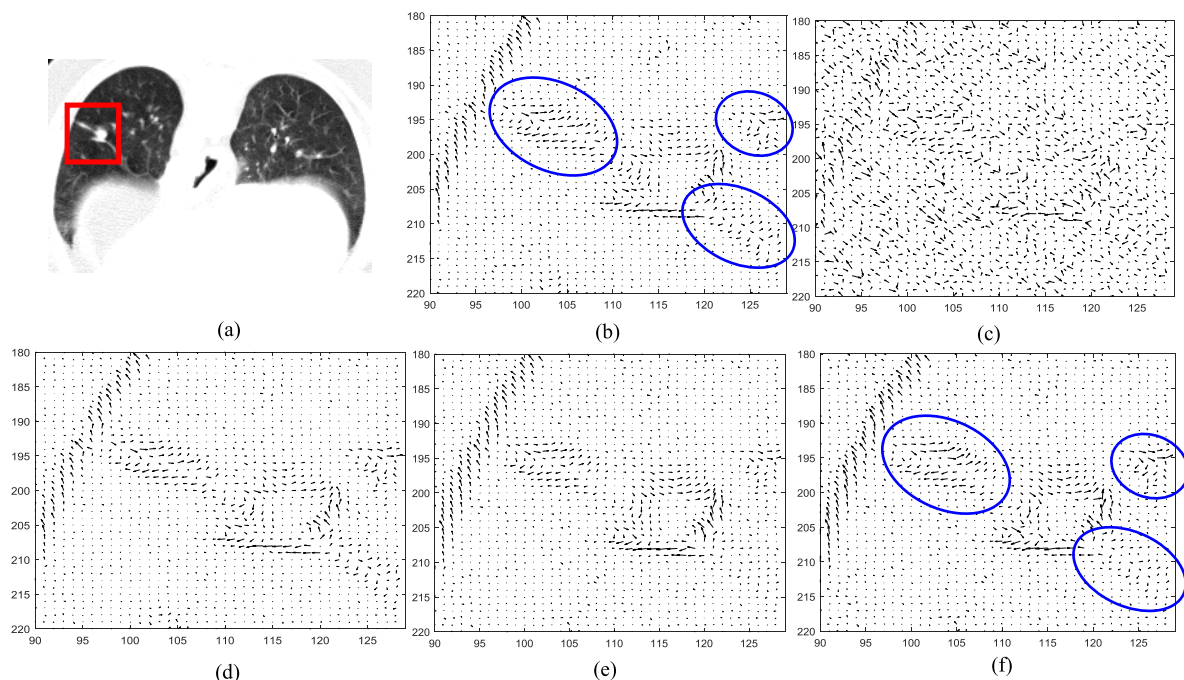
FIGURE 5. NVF images of the ROI for slice #22. The ROI is shown in (a) with red rectangle. (b)-(f) are corresponding to the FDCT-FBP, the LDCT-FBP, the images reconstructed with PWLS-ndiNLM, PWLS-NLM and PWLS-NLMpatch algorithms, respectively.

2) OFFLINE TRAINING DATABASE

To study the influence of offline training database μ^{DB} on PWLS-NLMpatch performance, we build a few training databases with different sizes and different positions extracted from FDCT #1 and/or #2. Firstly, the training database of total 1373530 2D patches, which is set as the

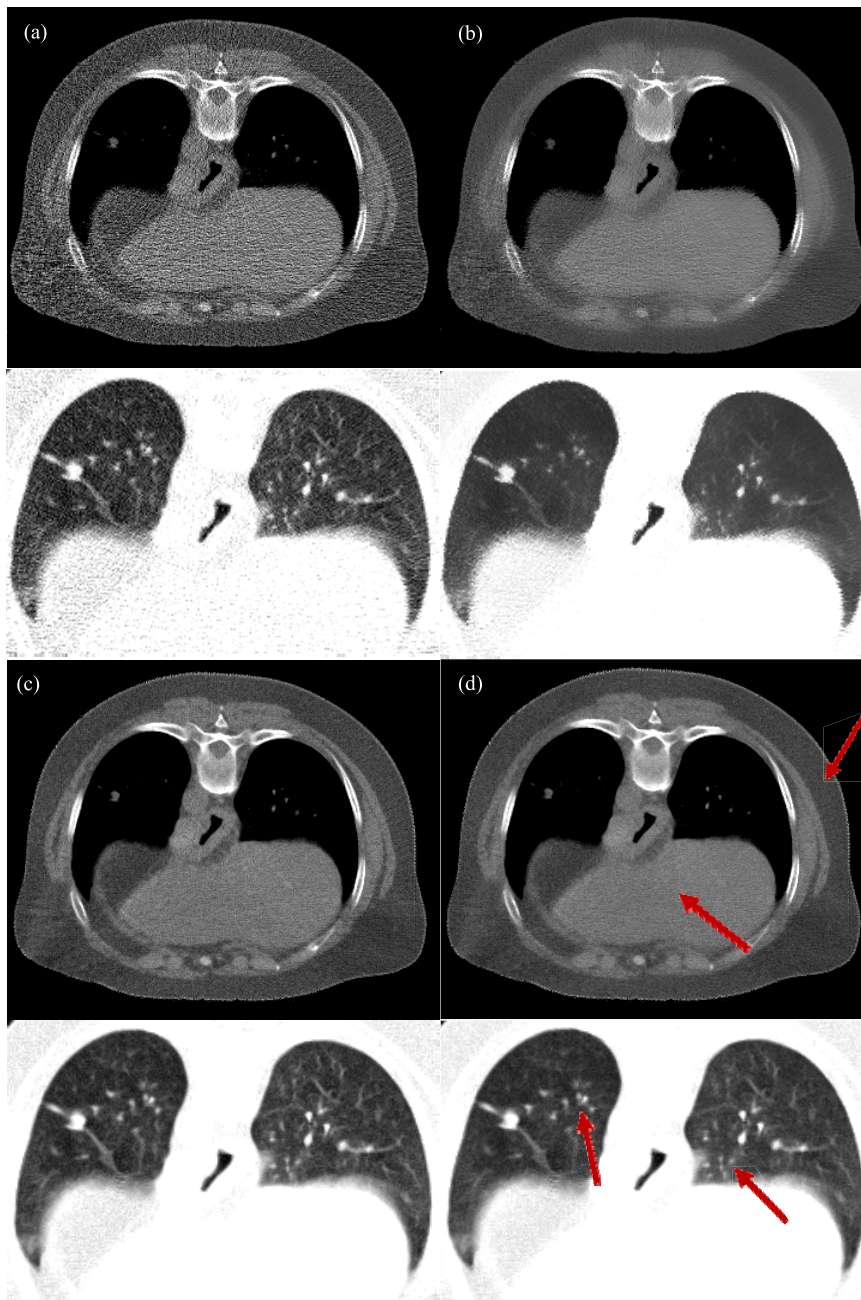**FIGURE 6.** Reconstructions by PWLS-NLMpatch algorithm with different initial images. (a) and (b) are the LDCT-FBP image, NLMimage, respectively. The PWLS-NLMpatch reconstructions using them as initial images are shown in (c) and (d) respectively. They are shown with a window of [0.0112, 0.0288] mm^{-1} for better displaying the mediastinum and bone structure. Their enlarged lung regions are shown on the next line with a lung display window of [0, 0.0220] mm^{-1}.

reference set, were constructed automatically with a sliding distance of one pixel on the manual cropping ten ROIs from ten interval slices with *odd* slice number from FDCT #1 and nine ROIs from nine interval slices with *odd* slice number from FDCT #2. Then for studying the effect of μ^{DB} size to the reconstruction, we chose a subset, consisting of 1%, 10%, 25%, 50% patches of the entire reference set, respectively, to form training databases of different sizes. Also, for

studying the effect of the source position of μ^{DB}, we chose ten interval slices with *even* numbers from FDCT #1 and nine interval slices with *even* numbers from FDCT #2 to construct the training database (total 1318138 2D patches). At last, considering both of the above factors, a training database from five interval slices only from FDCT #1 with 350709 2D patches (about 25% of the reference set size) were also applied to construct the training database. The RMSE

TABLE 3. The RMSE and UQI of the ROIs in slice #22 of Figure 2 using different training database sizes.

Merits	ROIs	Training database size (proportion to the reference set)				
		1%	10%	25%	50%	100%
RMSE	ROI1	8.37	7.98	7.90	7.85	7.83
(10^{-4})	ROI2	8.18	7.89	7.78	7.76	7.72
UQI	ROI1	1.9355	1.9432	1.9456	1.9469	1.9473
	ROI2	1.9237	1.9293	1.9317	1.9323	1.9333

TABLE 4. The RMSE and UQI of the ROIs in slice #22 of Figure 2 using different training database positions.

Merits	ROIs	Training database position		
		Ten interval slices with odd numbers from FDCT #1 and nine interval slices with odd numbers from FDCT #2	Ten interval slices with even numbers from FDCT #1 and nine interval slices with even numbers from FDCT #2	Five interval slices of FDCT #1
RMSE	ROI1	7.83	7.84	7.99
(10^{-4})	ROI2	7.72	7.62	7.71
UQI	ROI1	1.9473	1.9468	1.9430
	ROI2	1.9333	1.9351	1.9335

and UQI of the ROIs for slice #22 shown in Figure 1 with different training database sizes and different positions are listed in Table 3 and Table 4.

The RMSE and UQI merits in Table 3 show that the reconstruction with 25% patches of the entire reference training database are very close to the reconstruction with total 2D patches. The decreasing training database size will benefit for reducing the offline time of searching similar patches in step 3. So, about 25% patches of the entire reference training database were chosen for the PWLS-NLMpatch reconstruction.

The RMSE and UQI of Table 4 show that images reconstructed with similar size level of training databases, which are coming from different positions, are almost similar to each other in the two merits (columns 3-4). It illustrates that high-quality patches in the NLM prior will help improving the reconstruction performance, no matter where they come. Compared between columns 5 and columns 3-4, it shows that the RMSE and UQI of the images reconstructed with the training database constructed by five interval slices is comparable to that of the training database constructed by nineteen interval slices, which further illustrates 25% patches of the entire reference set (about hundreds of thousands of patches) is adequate for the PWLS-NLMpatch reconstruction.

3) RECONSTRUCTION PARAMETERS WITHIN PWLS-NLMpatch METHOD

There are several parameters related to the PWLS-NLMpatch method, including PW size, DBj size, standard deviation a of the Gaussian kernel, filtering parameter h, and smoothing parameter β. Then it is necessary to determine the optimal values.

a: THE PW SIZE AND A

The PW size and a do not have noticeable effects on the reconstructed image, so they were set at PW size $= 5 \times 5$

and $a = 5$, similar to the PWLS-ndiNLM or PWLS-NLM algorithms [20], [24], [30].

b: THE DB_J SIZE

The DB_j size is similar to the search window size of the PWLS-ndiNLM or PWLS-NLM algorithms. Researchers have reported that search window size $= 289$ (17×17) is good enough for LDCT reconstruction. Therefore, a typical selection of DB_j size $=300$ (about the same size) was used for all the cases in the study.

c: THE PARAMETERS H AND β

The parameters h and β together control the smoothness of the reconstruction. A few combinations of h and β were studied to determine the proper values. The h was set 3×10^5, 5×10^5, 7×10^5, 1×10^6 and 2×10^6. β was set 0.005 and 0.01. The RMSE and UQI for two ROIs of the lung for slice #22 were calculated (Table5) and plotted as the function of h and β (Figure 7). The criterion of the lowest RMSE and largest UQI were considered for determining the optimized parameters of h and β. Seen from Figure 7, the curves of different h have similar changing trend. The RMSE decreases firstly and then increases slowly with increased β, while the UQI has opposite tread, indicating that there is a best β for each h within a small common range. For both of the fixed h of 0.005 and 0.01, the best β was 1×10^6. So, we choose β of 1×10^6. The RMSE and UQI at h of 0.005 are better than that with h of 0.01. To test the variation when h decreased again, the performance of reconstruction with $h =0.003$, 0.002 and $\beta =1 \times 10^6$ was studied. The RMSE and UQI with parameters $h =0.003$ and $\beta =1 \times 10^6$ were a little better than the result when $h =0.005$, 0.002 and $\beta =1 \times 10^6$, which is listed in Table 5. So, h and β were reasonably set as 0.003 and 1×10^6, respectively for reconstructing slice #22. For other slices, β could be set in the range of 7×10^5 to 1×10^6 and h

TABLE 5. The RMSE and UQI of the ROIs in figure 2(a) with different *h* and *β* values.

| Merits	ROIs	$\beta=3\times10^5$		$\beta=5\times10^5$		$\beta=7\times10^5$		$\beta=1\times10^6$				$\beta=2\times10^6$	
		h=0.005	*h=0.01*	*h=0.005*	*h=0.01*	*h=0.005*	*h=0.01*	*h=0.002*	*h=0.003*	*h=0.005*	*h=0.01*	*h=0.005*	*h=0.01*
RMSE	ROI1	11.0	10.9	9.11	9.17	8.37	8.50	7.92	7.83	8.04	8.23	8.50	8.70
(10-4)	ROI2	9.95	9.90	8.54	8.55	7.98	8.04	7.81	7.72	7.75	7.89	8.19	8.47
UQI	ROI1	1.8884	1.8882	1.9252	1.9233	1.9386	1.9354	1.9454	1.9473	1.9438	1.9395	1.9327	1.9276
	ROI2	1.8959	1.8959	1.9204	1.9191	1.9291	1.9267	1.9320	1.9333	1.9323	1.9284	1.9218	1.9142
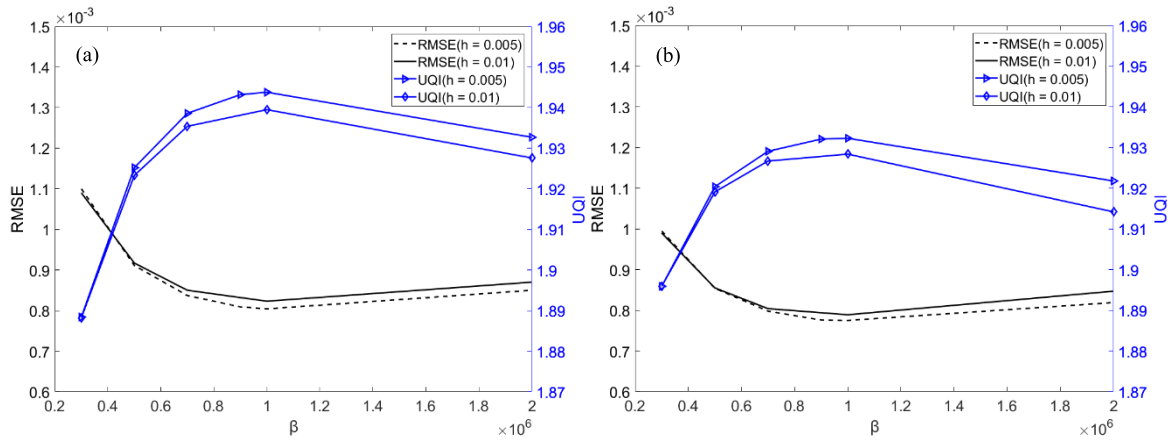
FIGURE 7. RMSE and UQI with different *h* and *β* of two ROIs of the PWLS-NLMpatch reconstructions for slice #22. (a) is for the first ROI and (b) is for another ROI.

be set in the range of 0.002∼0.01 with fine tuning depending on the noise condition.

IV. DISCUSSION

In this paper, a new NLM prior model with nonlocal weights determined by optimal similar patch samples from the FDCT database was proposed to improve the uLDCT reconstruction for Lung. The priori information about the local structure from FDCT can be incorporated into the model conveniently without registration. With this method, the FDCT data can come from large chest CT database, not limiting to the same patient. Reconstructions for uLDCT data had shown its potential in structure detail preservation. The performance of RMSE, UQI and NVF plot was better than that of PWLS-NLM algorithm in the lung ROIs, which demonstrated its superior reconstructions for low-dose lung data.

Reconstructing with multi parameters and their difficult determination is a common problem for iterative-type algorithms. For the proposed PWLS-NLMpatch algorithm, the more influential parameters of filtering parameter h, and smoothing parameter β were studied. Both of them control the smoothness of the reconstruction. The larger, the smoother of the images. Among them, β controls the tradeoff between the data fidelity term and the regularization term. In our study, β was set within a small range ($\beta = 7\times10^5$ to 1×10^6) by experiment for the reconstruction of lung

LDCT data with 10mAs, which was a little larger than most of that in the published papers [20], [28]. This was because mAs of the current in our study was smaller and larger β was needed to decrease the data fidelity for controlling the noise and artifacts. Parameter h was set 0.003 for all of the experiments, in which the reconstructions were acceptable. It controls the amount of de-noising and could be adjusted adaptively according to the noise situations. In our study, h was set to a constant value for all the NLM-type algorithms. Strategies to develop adaptive h will be studied for future research to further improve the presented scheme.

Except for the reconstruction parameters, the quality of initial image and the offline training database were also studied on their effect for the PWLS-NLMpatch performance. Obviously, if there were severe noises or artifacts in the initial image, the quality of the selective patch samples in the training database would be declined, for they were built up based on the similarity between the FDCT patches and the target patch of the initial image. Therefor it is better to improve the quality of initial image. The NLM filtering was used for denoising the LDCT-FBP image in our study and the reconstruction with the filtered image as the initial image was improved in reducing artifacts and noise. Other methods such as algorithms with data processing in sinogram domain will be tried in future research to further improve the initial image. To study the influence of offline training

database on PWLS-NLMpatch performance, a few training databases with different sizes and different positions were built up for the following reconstruction. Reconstructing with larger training database was good for RMSE and UQI merits. However, larger size of training database will cost much time in searching similar patches. Therefore, tests were done with different sizes of database, which showed that about 3.5×10^5 patches were enough for our tests (Table 3). Further tests with training databases from different positions (Table 4) demonstrated the performance of PWLS-NLMpatch with 25% patches of the reference set could be preserved, no matter what FDCT images they come from.

Although the proposed PWLS-NLMpatch has shown its improvement in RMSE, UQI, LSF and NVF, compared to the PWLS-NLM algorithm, it was worse than the PWLS-ndiNLM method. The results can be understood, as the FDCT itself has the best match to the LDCT image to be reconstructed. So, searching the best matching patches to the target patch is an essential problem for the PWLS-ndiNLM. Besides improving the initial image quality, optimizing the training database and the similar patch samples to the target patch is another interesting topic for studying. For example, the training database can be built up precisely by subdivided them into lung database, bone database and so on, according to segmented organs or tissues [31]. In addition, more methods will be tried for searching closer and adaptive patch samples to the target patch from the optimized training database.

One limitation of the study was the testing uLDCT data with 10mAs was produced by simulation. Since low dose CT projection is difficult to obtain, many studies are performed with simulated LDCT data [29], [32], [33]. In our simulation, we assume the detected photon intensity follows the Poisson process plus the electronic noise background [15]. The incident X-ray intensity and electronic noise for simulation comes from actual data collected. The simulation method has been verified in previous work [33]. It can be assumed that the data simulated are close to the real data. Suppose the effective dose of CT scanning is proportional to the tube current-time product, the effective dose with 10mAs is at least below 1.0 mSv. It is relatively low dose in existing lung screening trial or new algorithm studies. However, the preliminary study focuses on the methodological performance of the proposed algorithm and lacks clinical evaluation. It has been reported that the radiologist readers can still maintain the diagnostic performance with ∼96% dose reduction [32], which is very important for clinical application. Future study will strengthen this aspect of testing and do some assessment under much lower dose.

Another limitation was the proposed algorithm was tested only for one type of CT scanner and the FDCT images for building the training database were from the same CT scanner. More reconstructing will be implemented for testing the PWLS-NLMpatch algorithm for different CT scanner in future, especially when the training database and projection data are from different CT scanners. The computational burden is another drawback of the algorithm. Although the training database was built up offline, the multiple re-projection and back-projection operation cycles in the algorithm dominant the calculation process. However, with the development of fast computers and current GPU based methods [34], [35], the computation issue may be not a problem in the near future.

V. CONCLUSION

In summary, a new NLM prior model based on FDCT database was proposed in this paper. Preliminary reconstruction with LDCT data has shown its performance in reducing the noise, streaking artifacts and improving structure details. Reconstructions with 10mAs data in the study show the dose can drop below 1.0mSv with the proposed strategy, indicating its potential for uLDCT lung screening.

REFERENCES

[1] E. Bender, "Epidemiology: The dominant malignancy," *Nature*, vol. 513, pp. S2–S3, Sep. 2014.

[2] M. P. Coleman *et al.*, "Cancer survival in Australia, Canada, Denmark, Norway, Sweden, and the UK, 1995-2007 the international cancer benchmarking partnership: An analysis of population-based cancer registry data," *Lancet*, vol. 377, pp. 127–138, Jan. 2011.

[3] Q.-Y. Hong, G.-M. Wu, G.-S. Qian, C.-P. Hu, J.-Y. Zhou, L.-A. Chen, W.-M. Li, S.-Y. Li, K. Wang, Q. Wang, X.-J. Zhang, J. Li, X. Gong, and C.-X. Bai, "Prevention and management of lung cancer in China," *Cancer*, vol. 121, no. 17, pp. 3080–3088, 2015.

[4] J. K. Field, "Perspective: The screening imperative," *Nature*, vol. 513, p. S7, Sep. 2014.

[5] C. I. Henschke, D. I. McCauley, D. F. Yankelevitz, D. P. Naidich, G. McGuinness, O. S. Miettinen, D. M. Libby, M. W. Pasmantier, J. Koizumi, N. K. Altorki, and J. P. Smith, "Early lung cancer action project: Overall design and findings from baseline screening," *Lancet*, vol. 354, pp. 99–105, Jul. 1999.

[6] M. C. Tammemagi and S. Lam, "Screening for lung cancer using low dose computed tomography," *Proc. Brit. Med. J.*, vol. 348, May 2014, Art. no. g2253.

[7] C. I. Henschke, D. F. Yankelevitz, D. M. Libby, M. W. Pasmantier, J. P. Smith, and O. S. Miettinen, "Survival of patients with stage I lung cancer detected on CT screening," *England J. Med.*, vol. 355, pp. 1763–1771, Oct. 2006.

[8] D. Aberle, "Reduced lung-cancer mortality with low-dose computed tomographic screening," *New England J. Med.*, vol. 365, no. 5, pp. 395–409, 2011.

[9] C. I. Henschke. (2016). *International Early Lung Cancer Action Program: Screening Protocol.* [Online]. Available: http://www.ielcap.org/sites/default/files/I-ELCAP-protocol.pdf

[10] F. A. Mettler, W. Huda, T. T. Yoshizumi, and M. Mahesh, "Effective doses in radiology and diagnostic nuclear medicine: A catalog," *Radiology*, vol. 248, pp. 254–263, Jul. 2008.

[11] R. R. Gill, M. T. Jaklitsch, and F. L. Jacobson, "Controversies in lung cancer screening," *J. Amer. College Radiol.*, vol. 10, pp. 931–936, Dec. 2013.

[12] P. B. Bach, J. N. Mirkin, T. K. Oliver, C. G. Azzoli, D. A. Berry, and O. W. Brawley, "Benefits and harms of CT screening for lung cancer," *JAMA*, vol. 307, pp. 2418–2429, Jun. 2012.

[13] J. Hsieh, "Adaptive streak artifact reduction in computed tomography resulting from excessive X-ray photon noise," *Med. Phys.*, vol. 25, pp. 2139–2147, Nov. 1998.

[14] J. Wang, T. Li, H. Lu, and Z. Liang, "Penalized weighted least-squares approach to sinogram noise reduction and image reconstruction for low-dose X-ray computed tomography," *IEEE Trans. Med. Imag.*, vol. 25, no. 10, pp. 1272–1283, Oct. 2006.

[15] J. Ma, Z. Liang, Y. Fan, Y. Liu, J. Huang, W. Chen, and H. Lu, "Variance analysis of X-ray CT sinograms in the presence of electronic noise background," *Med. Phys.*, vol. 39, no. 7, pp. 4051–4065, 2012.

[16] J.-B. Thibault, C. A. Bouman, K. D. Sauer, and J. Hsieh, "A recursive filter for noise reduction in statistical iterative tomographic imaging," *Proc. SPIE*, vol. 6065, Feb. 2006, Art. no. 60650X.

[17] B. D. Man and J. Fessler, "Statistical iterative reconstruction for X-ray computed tomography," in *Biomedical Mathematics: Promising Directions in Imaging, Therapy Planning, and Inverse Problems*. Madison, WI, USA: Medical Physics Publishing, 2010, pp. 113–140.

[18] J. Tang, B. E. Nett, and G.-H. Chen, "Performance comparison between total variation (TV)-based compressed sensing and statistical iterative reconstruction algorithms," *Phys. Med. Biol.*, vol. 54, no. 19, p. 5781, Oct. 2009.

[19] Q. Xu, H. Yu, X. Mou, L. Zhang, J. Hsieh, and G. Wang, "Low-dose X-ray CT reconstruction via dictionary learning," *IEEE Trans. Med. Imaging*, vol. 31, no. 9, pp. 1682–1697, Sep. 2012.

[20] H. Zhang, J. Ma, J. Wang, Y. Liu, H. Lu, and Z. Liang, "Statistical image reconstruction for low-dose CT using nonlocal means-based regularization," *Computerized Med. Imag. Graph.*, vol. 38, pp. 423–435, Sep. 2014.

[21] H. Zhang, H. Han, Z. Liang, Y. Hu, Y. Liu, W. Moore, J. Ma, and H. Lu, "Extracting information from previous full-dose CT scan for knowledge-based Bayesian reconstruction of current low-dose CT images," *IEEE Trans. Med. Imag.*, vol. 35, no. 3, pp. 860–870, Mar. 2016.

[22] H. Zhang, H. Han, J. Wang, J. Ma, Y. Liu, W. Moore, and Z. Liang, "Deriving adaptive MRF coefficients from previous normal-dose CT scan for low-dose image reconstruction via penalized weighted least-squares minimization," *Med. Phy.*, vol. 41, no. 4, 2014, Art. no. 041916.

[23] D. Karimi and R. K. Ward, "Patch-based models and algorithms for image processing: A review of the basic principles and methods, and their application in computed tomography," *Int. J. Comput. Assist. Radiol. Surg.*, vol. 11, pp. 1765–1777, Oct. 2016.

[24] H. Zhang, J. Ma, J. Wang, Y. Liu, H. Han, H. Lu, W. Moore, and Z. Liang, "Statistical image reconstruction for low-dose CT using nonlocal means-based regularization. Part II: An adaptive approach," *Computerized Med. Imag. Graph.*, vol. 43, pp. 26–35, Jul. 2015.

[25] J. Ma, H. Zhang, Y. Gao, J. Huang, Z. Liang, Q. Feng, and W. Chen, "Iterative image reconstruction for cerebral perfusion CT using a pre-contrast scan induced edge-preserving prior," *Phys. Med. Biol.*, vol. 57, no. 2, p. 7519, 2012.

[26] J. Ma, J. Huang, Q. Feng, H. Zhang, H. Lu, and Z. Liang, "Low-dose computed tomography image restoration using previous normal-dose scan," *Med. Phys.*, vol. 38, pp. 5713–5731, Oct. 2011.

[27] Y. Zhang, J. Rong, H. Lu, Y. Xing, and J. Meng, "Low-dose lung CT image restoration using adaptive prior features from full-dose training database," *IEEE Trans. Med. Imag.*, vol. 36, no. 12, pp. 2510–2523, Sep. 2017.

[28] H. Zhang, J. Huang, J. Ma, Z. Bian, Q. Feng, H. Lu, Z. Liang, and W. Chen, "Iterative reconstruction for X-ray computed tomography using prior-image induced nonlocal regularization," *IEEE Trans. Biomed. Eng.*, vol. 61, no. 9, pp. 2367–2378, Sep. 2014.

[29] Y. Liu, J. Ma, Y. Fan, and Z. Liang, "Adaptive-weighted total variation minimization for sparse data toward low-dose X-ray computed tomography image reconstruction," *Phys. Med. Biol.*, vol. 57, p. 7923, Dec. 2012.

[30] H. Zhang, J. Ma, J. Wang, W. Moore, and Z. Liang, "Assessment of prior image induced nonlocal means regularization for low-dose CT reconstruction: Change in anatomy," *Med. Phys.*, vol. 44, pp. e264–e278, Sep. 2017.

[31] Y. Gao, Z. Liang, W. Moore, H. Zhang, M. J. Pomeroy, J. A. Ferretti, T. V. Bilfinger, J. Ma, and H. Lu, "A feasibility study of extracting tissue textures from a previous full-dose CT database as prior Knowledge for Bayesian reconstruction of current low-dose CT images," *IEEE Trans. Med. Imag.*, vol. 38, no. 8, pp. 1981–1992, Aug. 2019.

[32] J. G. Fletcher, L. Yu, J. L. Fidler, D. L. Levin, D. R. DeLone, D. M. Hough, N. Takahashi, S. K. Venkatesh, A.-M. G. Sykes, D. White, R. M. Lindell, A. L. Kotsenas, N. G. Campeau, V. T. Lehman, A. C. Bartley, S. Leng, D. R. Holmes, A. Y. Toledano, R. E. Carte, and C. H. McCollough, "Estimation of observer performance for reduced radiation dose levels in CT: Eliminating reduced dose levels that are too low is the first step," *Academic Radiol.*, vol. 24, pp. 876–890, Jul. 2017.

[33] D. Zeng, J. Huang, Z. Bian, S. Niu, H. Zhang, Q. Feng, Z. Liang, and J. Ma, "A simple low-dose X-ray CT simulation from high-dose scan," *IEEE Trans. Nucl. Sci.*, vol. 62, no. 5, pp. 2226–2233, Oct. 2015.

[34] P. Després and X. Jia, "A review of GPU-based medical image reconstruction," *Phys. Medica*, vol. 42, pp. 76–92, Oct. 2017.

[35] S. Ha and K. Mueller, "A look-up table-based ray integration framework for 2-D/3-D forward and back projection in X-ray CT," *IEEE Trans. Med. Imag.*, vol. 37, no. 2, pp. 361–371, Feb. 2018.

WENLEI LIU received the M.S. degree in computer applications technology and the Ph.D. degree in biomedical engineering from Fourth Military Medical University, in 2013 and 2017, respectively. He is currently an Assistant Engineer with the Department of Medical Engineering, General Hospital of Western Theater Command. He is interested in CT imaging technology and its clinical applications.

PENG GAO received the M.S. degree in biomedical engineering from Fourth Military Medical University, in 2016, and where he is currently pursuing the Ph.D. degree. His research interests include low-dose CT imaging and multimodality imaging.

YUANKE ZHANG received the Ph.D. degree in computer application technology from Xidian University, China, in 2011. After graduation, he joined Qufu Normal University. From June 2016 to August 2018, he was involved in a Postdoctoral research with the School of Biomedical Engineering, Fourth Military Medical University. He is currently a Postdoctoral Researcher with the School of Biomedical Engineering, Southern Medical University. His research interests include theory and methods of PET/CT image reconstruction, and low-dose CT image reconstruction and restoration.

TIANSHUAI LIU received the M.S. degree in mechanical engineering from the PLA University of Science and Technology, in 2015, and the Ph.D. degree in biophysics from Fourth Military Medical University, in 2018. He is currently a Lecturer with the Department of Biomedical Engineering, Fourth Military Medical University, China. His current research interests include X-ray imaging model and image reconstruction techniques.

HUANGSHENG PU received the M.S. degree from Fourth Military Medical University and the Ph.D. degree from Tsinghua University. His current research interests include optical molecular imaging, fluorescence molecular tomography, and super-resolution fluorescence microscopic imaging.

JUNYAN RONG received the Ph.D. degree in physics from the Institute of High Energy Physics, Chinese Academy of Sciences, Beijing, China, in 2009. From 2009 to 2012, she has been an Assistant Professor with the Paul Lauterbur Center for Biomedical Imaging Research, Shenzhen Institutes of Advanced Technology, Chinese Academy of Sciences, Shenzhen, China. She is currently an Assistant Professor with Fourth Military Medical University. Her research interests include low-dose CT imaging, reconstruction algorithm, and multimodality imaging.

HONGBING LU received the B.S. and M.S. degrees in biomedical engineering from Xi'an Jiaotong University, in 1988 and 1991, respectively, and the Ph.D. degree in biomedical engineering from Tsinghua University, China, in 1998, followed by a Postdoctoral training in radiology with the State University of New York, Stony Brook, until 2002. She is currently a Professor with the Department of Biomedical Engineering, Fourth Military Medical University, China. She has authored or coauthored over 100 peer-reviewed journal articles, books, and numerous conference papers. She holds more than 10 U.S. and Chinese patents in which half have been licensed. She is the Principal Investigator of over fifteen projects funded by the National Science Foundation of China, Ministry of Science and Technology, and the Military Research Foundation. Her research interests include spectrum from medical image reconstruction to image analysis for computer-aided detection (CADe) and diagnosis (CADx).

• • •